The morphology and composition of nanosized amorphous-phase separation in the Y2O3–Al2O3–SiO2 glass system

Jan Baborák, Petr Vařák, Aurélien Canizarès, Miroslav Rada, Cécile Genevois, Michael J Pitcher, Emmanuel Véron, Alessio Zandonà, Mathieu Allix, Pavla Nekvindová

The morphology and composition of nanosized amorphous-phase separation in the Y_2O_3-Al_2O_3-SiO_2 glass system

Jan Baborák[1,2], Petr Vařák[1], Aurélien Canizares[2], Miroslav Rada[3], Cécile Genevois[2], Michael J. Pitcher[2], Emmanuel Véron[2], Alessio Zandonà[2,*], Mathieu Allix[2], Pavla Nekvindová[1]

[1] *Department of Inorganic Chemistry, University of Chemistry and Technology, Technická 5, 166 28, Prague, Czech Republic*

[2] *CEMHTI – CNRS UPR3079, 1 Av. de la Recherche Scientifique, 45100 Orléans, France*

[3] *Department of Glass and Ceramics, University of Chemistry and Technology, Technická 5, 166 28, Prague, Czech Republic*

**Corresponding author:* alessio.zandona@tu-clausthal.de

Abstract

A systematic experimental study of the Y_2O_3-Al_2O_3-SiO_2 (YAS) compositional system has been carried out with a focus on nanoparticle formation in the high SiO_2 region, where nanoscale phase separation occurs. The unique capabilities of the aerodynamic levitation coupled to the laser-heating method have been exploited and compared to conventional melt-quenching. This systematic study has mainly focused on the region where melting temperatures exceed 1700°C, which is the maximum temperature commonly available for the preparation of glass by conventional melt-quenching. The feasibility and the effect of the two synthesis routes on the preparation of glass samples have been compared. The prepared samples were characterised by X-ray diffraction, differential scanning calorimetry, Raman spectroscopy, and scanning and transmission electron microscopy. It is evident from the results that in the part of the phase diagram with SiO_2 content above 65 mol% and simultaneously Y_2O_3 content below 17.5 mol%, the phase separation has led to the formation of amorphous SiO_2 nanoparticles. It has been shown that the size and distribution of the nanoparticles can be controlled not only by the chosen technology but also by changing the starting composition.

Keywords: silicate glass, YAS, phase separation, aerodynamic levitation, nanoparticles

1. Introduction

Composites or glass-ceramic materials based on an inorganic-oxide amorphous matrix containing crystalline or glassy nanoparticles (e.g. metallic, perovskite, spinel…) with different compositions currently find wide application [1–3]. In recent years, many efforts have been devoted, for example, to the preparation of full-volume luminescence optical devices containing nanoparticles such as broadband

optical amplifiers, transition-metal-doped glass-ceramics for tuneable laser materials or optical fibres with properties modified by the introduction of luminescent nanocrystals [4,5]. Transparent polycrystalline ceramics have demonstrated the ability to replace the commonly used single crystals in electronics and scintillation devices in addition to optics [6,7]. With a focus on the controlled crystallisation of oxide nanoparticles, numerous transparent materials containing oxide nanoparticles of Al_2O_3 [8,9], Sc_2O_3 [10], ZrO_2 [11–13], ZnO [14,15] or SnO_2 [16] have been created in glass matrices. More complex transparent oxide nano-glass-ceramic materials such as spinels (e.g. $ZnGa_2O_4$) have also been developed [17–21]. These research studies have demonstrated that the glass-ceramic route offers a great opportunity to design new nanostructured materials with a wide range of tuneable optical properties. However, the carefully controlled preparation of transparent glass-ceramics (or of nanostructured glass) with uniform size and distribution of nanoparticles is not easy and is currently a challenge for the scientific community.

The Y_2O_3-Al_2O_3-SiO_2 (YAS) glass system has been the subject of intensive investigation over the past decade due to its great importance in optical applications, along with its outstanding physical and chemical stability [22,23]. Moreover, these materials can be very easily associated with SiO_2-based optical fibres and also doped with lanthanides as well as other lasing elements [24–26]. From this point of view, the area with a high SiO_2 content, similar in composition to commonly used silica-based fibres, is very interesting. According to the experimental studies available [27,28], it could be assumed that glass formation occurs for compositions in the middle of the diagram. Based on the phase diagrams available [28–33], crystalline phases such as Y_2O_3, Al_2O_3, SiO_2, yttrium-aluminium garnet (YAG), yttrium-aluminium perovskite (YAP), Y_2SiO_5, $Y_2Si_2O_7$ and mullite occur in areas with a high concentration of one of the oxides. So far, glass crystallisation has been examined in this system [34–40], but the SiO_2-rich portion of the ternary phase diagram has not been thoroughly explored. The reason is the difficult preparation of materials with melting temperatures above 1700 °C and relatively high viscosity, which make it impossible to use the melt-quenching method in a conventional furnace and to cast homogeneous samples.

To prepare the samples, we used aerodynamic levitation coupled to laser heating (ADL), which is an experimental technique suitable for the preparation of glass samples with unusual chemical compositions [41–43]. This technology enables the preparation of glass systems with very high melting points and subsequent relatively fast cooling of the material. Like such methods as metal-organic chemical vapour deposition (MOCVD), spark plasma deposition or sol-gel technique, it offers the possibility to prepare glassy material with high SiO_2 content. Its disadvantage is the formation of very small samples, which are spherical and 1–2 mm in diameter. However, the method offers conditions similar to those achieved in the drawing of optical fibres (melting temperature of 1900–2300 °C and a high cooling rate exceeding 1000 °C s^{-1} [44]) and is extremely suitable for the exploration of new compositional domains.

In this study, we have thus focused on the preparation of a set of YAS samples with SiO_2 content ranging from 35 to 95 mol%. We have particularly investigated the region with SiO_2 content above 80 mol%, varying the Y/Al ratio. The occurrence of phase separation in this region has been observed and described. The possibility of influencing the size and distribution of demixed droplets by the selection of a suitable composition has also been investigated. Our aim was to investigate experimentally the formation, composition and structure of nanoparticles in a high SiO_2-content region and to control their distribution and size by changing the glass composition.

2. Experimental

2.1. Sample preparation

Glass samples of the general composition $xY_2O_3.yAl_2O_3.zSiO_2$ (mol%) were prepared in our experiments using two glass-preparation methods (**Figure 1**): first, the common melt-quenching procedure and, second, aerodynamic levitation coupled to laser heating (ADL). The nominal glass compositions as well as sample names are summarised in **Table 1**. Moreover, the glass compositions are also plotted in the ternary phase diagram in **Figure 2**.

Melt-quenching preparation – The precursors used for the preparation of the glass were Y_2O_3 (Sigma-Aldrich, 99.9 wt% by XRF analysis); aluminium hydroxide, $Al(OH)_3$ (Lach-Ner, p.a.); silica gel, SiO_2 (Sigma-Aldrich, high-purity grade). The components were weighed to obtain 25 g of the final bulk glass and mixed. After that, the mixture of precursors was milled in a Retsch 100 planetary agate ball mill. Approximately 30 g of precursors, 30 g of agate milling spheres and 60 ml of demineralised water were put into a 125-ml agate milling vessel. The mill was set to 500 RPM for 10 min. The milled precursors were then filtered using a vacuum pump and dried in a laboratory dryer at 100°C overnight. The following day, the dry and milled glass batch was placed in a Pt80Rh20 crucible and melted in a high-temperature furnace at 1500–1650 °C for 4 hours. During the melting process, the glass was homogenised seven times by taking the crucible out of the furnace and making swirling motions while holding the crucible with tongs according to [45].

Four hours after the start of melting, part of the glass was cast into a steel mould, flattened with a steel rod, and quickly transferred into a preheated annealing furnace. The rest of the glass was returned to the melting furnace for 10 minutes and then rapidly quenched to produce shards by submerging the crucible into water. The crucible was handled with care not to let any water come into contact with the glass inside the crucible. After this, the shards were transferred to the annealing furnace as well. The annealing furnace was set to hold 700 °C for 120 min and then cooled to room temperature at the rate of 1°C min^{-1}.

Table 1 *– A summary of the nominal compositions (mol%) of the glasses prepared. The sample-code column summarises the chemical composition of the glass batch in mol%, rounded mathematically.*

Sample no.	***Sample code***	**x** (Y_2O_3)	**y** (Al_2O_3)	**z** (SiO_2)
1	*Y15-A50-S35*	15.0	49.8	35.2
2	*Y11-A35-S54*	10.7	35.4	53.9
3	*Y07-A24-S68*	7.3	24.2	68.5
4	*Y05-A15-S80*	4.6	15.3	80.1
5	*Y02-A08-S90*	2.4	7.9	89.7
6	*Y22-A32-S46*	21.9	32.4	45.7
7	*Y24-A22-S54*	23.5	22.3	54.2
8	*Y24-A14-S62*	24.5	13.5	62.0
9	*Y13-A19-S68*	12.6	19.2	68.2
10	*Y14-A11-S75*	14.0	10.6	75.4
11	*Y08-A12-S80*	7.9	12.1	80.0
12	*Y06-A09-S85*	6.0	9.0	85.0
13	*Y04-A06-S90*	4.0	6.0	90.0
14	*Y02-A03-S95*	2.0	3.0	95.0
16	*Y15-A05-S80*	15.0	5.0	80.0
18	*Y18-A03-S80*	17.5	2.5	80.0
22	*Y10-A10-S80*	10.0	10.0	80.0
23	*Y03-A18-S80*	2.5	17.5	80.0
33	*Y12-A22-S66*	12.2	22.0	65.8
34	*Y01-A25-S74*	1.0	25.0	74.0
35	*Y03-A25-S72*	3.0	25.0	72.0
36	*Y01-A15-S84*	1.0	15.0	84.0

ADL preparation – The chemicals used for the preparation of the glass using this technique were Y_2O_3 (Strem chemicals, 99.9 wt%); Al_2O_3 (Alfa Aesar, 99.97 wt%); SiO_2 (Alfa Aesar, 99.5 wt%). The components were weighed to obtain 1 g of the desired chemical composition, mixed in ethanol in an agate mortar, dried and then pressed into a coin shape using a 13-mm die and a hydraulic press. Subsequently, a small piece of this compressed sample (~50 mg) was placed into a conical nozzle of the ADL device (see **Figure 1**), levitated by a stream of Ar and melted at 1600–1900 °C by a pair of CO_2 lasers for 60 seconds. Such a prepared sample – a spherical glass bead with diameter of ~1–2 mm – was then rapidly cooled by the stream of Ar (~300°C/s) after switching off the lasers. Detailed description

of this synthesis technique was provided elsewhere [42,43]. Notice that the YAS system, also based on a previous fundamental study [43], is expected to be only slightly sensitive to high-temperature vaporization (XRF analysis performed elsewhere on similar samples never exhibited deviations above 2 wt% of each oxide).

2.1. The characterisation of the samples

Room-temperature powder X-ray diffraction analysis (XRD)

One to three beads or small pieces of bulk glass were crushed into fine powder in an agate mortar. Room-temperature powder X-ray diffraction (XRD) was performed using a Bruker D8 Advance laboratory diffractometer (Cu $K_{\alpha 1,2}$ radiation) equipped with a LynxEye XE detector in Bragg–Brentano geometry. Data were collected between 15° and 70° (2θ) with a 0.103° step size. The samples were dispersed on low-background flat Si holders by means of some ethanol droplets.

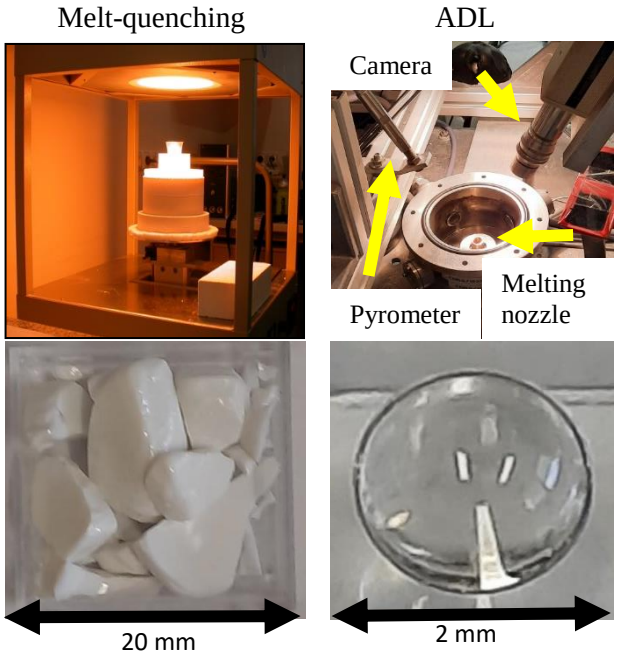

Figure 1 *A comparison of melt-quenching and ADL.*

Raman spectroscopy

The beads were embedded in epoxy pellets, which were then cut and polished using conventional SiC papers (P300-P4000) and diamond-particle suspensions. Subsequently, the beads were characterised at room temperature by Raman spectroscopy on a Renishaw InVia Qontor spectrometer mounting a green laser (514 nm) operated at 50 mW (power at the source). The signal was collected in the range of 80–2000 cm^{-1} (low-wavenumber cutoff of the edge filter: ~100 cm^{-1}) using a holographic grating of 1800 lines/mm, with 15-s acquisition time and six repetitions. Spectra were acquired after focusing 20–40 μm below the surface with a 50x objective from three samples/locations to ensure reproducibility. The

resulting Raman spectra were then averaged. The spectra were identically processed and compared using the Origin software, i.e. the baseline was manually selected based on the selection of 8–10 points and the spectra were graphically compared. The intensity of the spectra of melt-quenched samples (**9** and **10**) was normalised to the same level as the corresponding ADL samples.

Differential scanning calorimetry (DSC)

DSC was used to obtain information about the glass transition temperature T_g and the lowest crystallisation temperature T_c. Ten to twenty beads were crushed into fine powder in an agate mortar before analyses. Approximately 400 mg of each sample were analysed by a Setaram MHTC96 instrument. A 700 µl Pt crucible and Ar atmosphere were used for the DSC analyses. The heating rate of the samples was 10°C min^{-1}, and the analyses were conducted in the temperature range of 100–1400°C.

Scanning electron microscopy (SEM)

Prior to analyses with SEM, sample chips were embedded in epoxy resin, polished, and carbon-coated (15–20 nm) under vacuum. Microstructural analysis was carried out with an IT800SHL JEOL scanning electron microscope (FEG SEM) equipped with an SSD Ultim Max 100mm^2 detector (EDS Oxford system).

Transmission electron microscopy (TEM)

Most samples for transmission electron microscopy (TEM) were prepared from powder dispersed in absolute ethanol and deposited onto a holey carbon film supported by a copper grid. Bright-field images were acquired with a TEM (Philips CM20) operating at 200 kV.

On the samples **12**, **16** and **22**, selected-area electron diffraction (SAED), transmission electron microscopy (TEM) imaging and energy dispersive X-ray spectroscopy (EDS) elemental analysis were performed on a JEOL ARM200F (JEOL Ltd.) Cold FEG (Field Emission Gun) transmission electron microscope operating at 80 kV, equipped with a double spherical aberration corrector and fitted with a JEOL SDD CENTURIO EDS system. The sample **22** was first prepared by mechanical polishing with a tripod and inlaid diamond discs to reach the thickness of 40 µm. Thin foil was then obtained by argon ion milling (Gatan PIPS), by gradually reducing the incident beam voltage from 5 keV to 100 eV to remove beam-induced amorphisation. For the samples **12** and **16**, fine powders were first homogeneously dispersed in ethanol, after which one droplet of this suspension was deposited on a TEM amorphous holey carbon-coated copper grid and left to dry.

3. *Results*

3.1. A general description of the samples prepared

Glasses of various compositions were prepared by ADL, and the individual samples already differed in their optical appearance. All glasses with SiO_2 content below 70 mol% as well as some glasses with SiO_2 content above 70 mol% and simultaneously containing high amounts of Al_2O_3 were transparent (yellow circles in **Figure 2**). Glasses containing a high amount of SiO_2 and Y_2O_3 were opaque-white in appearance (red symbols in **Figure 2**). Two glass compositions, the samples **22** (*Y10-A10-S80*) and **14** (*Y02-A03-S95)*, showed distinct opalescence and are marked in orange.

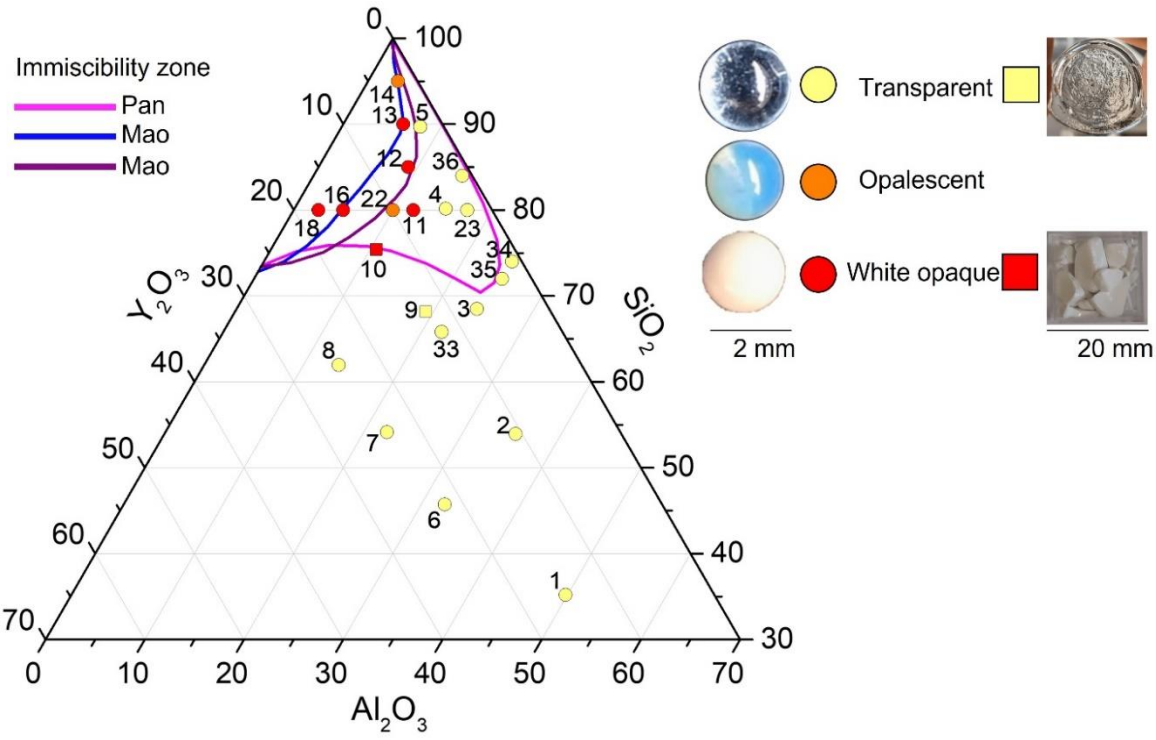

Figure 2 *Part of the YAS ternary diagram with highlighted stable liquid–liquid immiscibility fields, which were published by Pan et al. [29] and Mao et al. [33]. The samples prepared in this work by ADL are represented as circles: yellow = transparent, orange = opalescent, red = opaque white. The samples prepared by both melt-quenching and ADL are represented with squares. The diagram is accompanied by photographs of samples prepared by both techniques.*

For comparison, a transparent sample (composition **9** (*Y13-A19-S68*)) and a white opaque one (composition **10** (*Y14-A11-S75*)) were also prepared by the conventional melt-quenching technique, resulting in the same optical appearance as by ADL. These types of glass are marked with squares with the colour corresponding to their appearance. In addition, the liquid–liquid immiscibility regions theoretically calculated by Pan et al. [29] and Mao et al. [33] have been added to **Figure 2**.

3.2. The investigation of thermal properties and glass structure

The properties of the transparent glass samples labelled as **1–9** prepared by ADL were analysed by DSC. The glass transition temperature (T_g) and temperature at which the maximum of the first crystallisation peak occurs (T_c) were determined. One illustrative DSC curve (sample **1**(*Y15-A50-S35*)) is shown in **Figure 3a**. In **Table 2**, the determined values of T_g and T_c are shown for all individual types of glass. The T_g values range from 899 to 922 °C, with a difference of only 25 °C and no observable trends. More differences could be observed instead in the case of T_c: as plotted in **Figure 3b**, they increase with the addition of silica, as expected, while effect of the Y_2O_3 and Al_2O_3 addition is negligible.

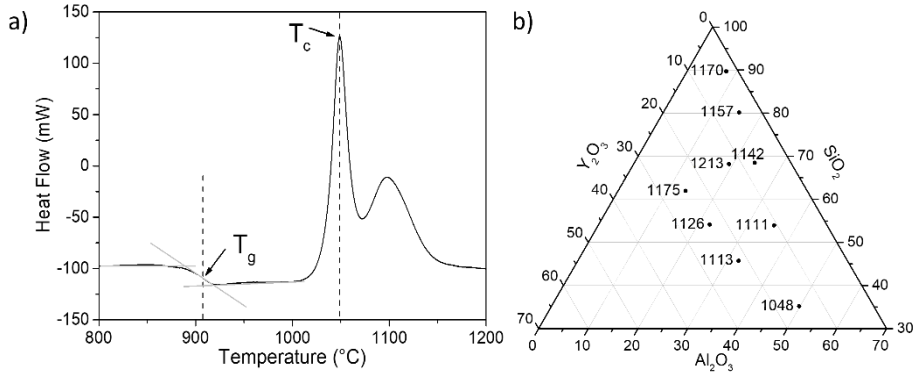

Figure 3 *The thermal behaviour of the glass samples determined by DSC analyses – (a) DSC curve measured for the sample 1(Y15-A50-S35) as an example; (b) part of the YAS ternary diagram showing the dependence of T_c (°C) on glass composition.*

Table 2 *Values of transformation and crystallisation temperatures. Estimated uncertainty: ± 5 °C.*

Glass		***T_g(°C)***	***T_c(°C)***
1	*Y15-A50-S35*	908	1048
2	*Y11-A35-S54*	903	1111
3	*Y07-A24-S68*	922	1142
4	*Y05-A15-S80*	919	1157
5	*Y02-A08-S90*	904	1170
6	*Y22-A32-S46*	899	1113
7	*Y24-A22-S54*	907	1126
8	*Y24-A14-S62*	918	1175
9	*Y13-A19-S68*	917	1213

To verify the possible formation of crystalline phases during quenching, quenched samples with the composition **1–10** were characterised using powder XRD. The observations focused mainly on the comparison between transparent and white opaque samples prepared by both methods. **Figure 4** shows the XRD pattern comparison for samples with the compositions **9** (*Y13-A19-S68*) and **10** (*Y14-A11-S75*)

(other measurements are not shown). It is obvious from the patterns that, regardless of their appearance, the samples have been confirmed to be amorphous, showing only the broad diffraction "hump" that is characteristic of silicate amorphous structures.

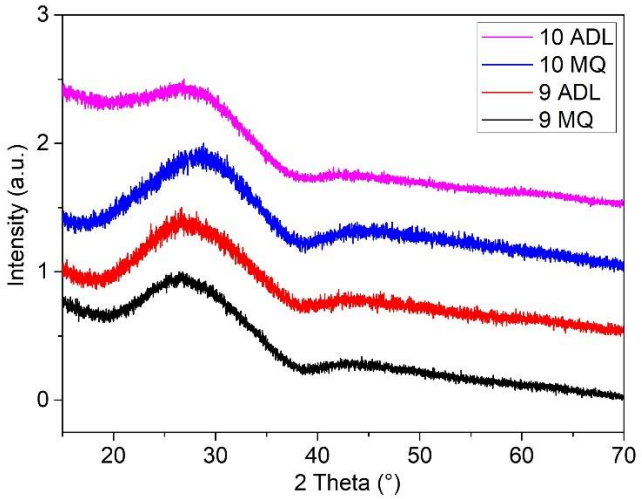

Figure 4 *The XRD pattern of the samples* ***9*** *(Y13-A19-S68) and* ***10*** *(Y14-A11-S75) prepared by melt quenching (MQ) as well by aerodynamic levitation coupled to laser heating technique (ADL).*

The structure of the YAS glass and network polymerisation are expected to be strongly dependent on composition, because of the variable role of the three oxide components. According to Christie et al. [46], the structure of YAS glass is that of a disordered glass network containing silicon and aluminium as network-forming cations and yttrium as a network-modifying cation. While silicon is entirely four-coordinated, aluminium ranges from four- to six-coordinated (NMR studies in [47]), and yttrium can have a wider range of coordination numbers, with six and seven being most common. Increasing the yttrium content increases all cation-oxygen coordination numbers and gives a greater range of oxygen environments. Most oxygen atoms have two, three or four neighbours, depending on composition, and the concentration of non-bridging oxygen atoms increases with increasing yttrium concentration. Increasing the yttrium concentration reduces the silicate network connectivity and reduces the clustering of the modifying yttrium atoms; both effects accelerate glass dissolution [48].

The glass structure changes have been studied by Raman spectroscopy. **Figure 5a** shows the Raman spectra of the glass samples **1–10** measured in the range of 200–1500 cm^{-1}. In the spectra, it is possible to see two distinct intensity regions, which are characteristic of alumino-silicate glass. A high-frequency contribution (A_{1000}) has been observed between 800 and 1200 cm^{-1}, with the main maximum in the range of 932–1057 cm^{-1}, depending on the type of the glass. This complex intensity envelope is known to arise from asymmetric Si-O-Si stretching vibrations in Q^n units, where Q represents [SiO_4] tetrahedra and *n* represents the number of bridging oxygens (BO). The high intensity of this band is typically present in highly depolymerised silicate glass containing network modifiers, such as alkali ions [49–51]. The

position of this band and the relatively low intensity in the samples **3** (*Y07-A24-S68*), **4** (*Y05-A15-S80*) and **5** (*Y02-A08-S90*) (see **Figure 5** – the red colour) is in good agreement with their high content of SiO_2. The positional shift of the band to lower wavenumbers and the increase of the intensity (with the maximum around 960 cm^{-1}) are caused by the breakdown of the silica network and by the interlinking of the Si-O-Al network; they can correspond to the lower content of SiO_2 and the higher content of both Al_2O_3 and Y_2O_3. This means that this band can be attributed to the stretching vibration of silicon-oxygen tetrahedra with two corners shared with aluminium (also yttrium) polyhedra [52].

The broad Raman band (A_{500}) with the maximum of the main peak between 394 and 477 cm^{-1} is related to the bending vibrations of the interconnected aluminosilicate network. Especially, the vibrations between 391 and 650 cm^{-1} are caused by the bending vibration of the bridging oxygen (BO) bonds of [SiO_4] units, and the band near 779 cm^{-1} could be assigned to the Si-O-Si network or to [AlO_4] units with three BOs and one non-bridging oxygen [53]. Significantly high intensity of these bands is evident in the samples **3** (*Y07-A24-S68*), **4** (*Y05-A15-S80*) and **5** (*Y02-A08-S90*) with a high content of SiO_2 and thus a high content of BOs between [SiO_4] tetrahedra. On the contrary, the samples **2** (*Y11-A35-S54*) and **6** (*Y22-A32-S46*) show a much lower relative intensity of this band, which can be ascribed to a decrease of Si-O-Si linkage due to a low content of SiO_2 and a high content of Y_2O_3 and Al_2O_3. This may be attributed to the fact that Al can also be present as five- or six-fold coordinated in the glass matrix and act as a modifier (like Y^{3+}) [54].

If we compare the spectra of the glass samples with the compositions **9** (*Y13-A19-S68*) (transparent) and **10** (*Y14-A11-S75*) (opaque), it is obvious at first glance that the positions of their bands are not very different. However, in detailed spectra (see **Figure 5b**), two new bands become visible in samples with the composition **10** (*Y14-A11-S75*), i.e. in opaque glass (due to phase separation, see below). The same peaks have been observed in the samples prepared by melt-quenching (not shown).

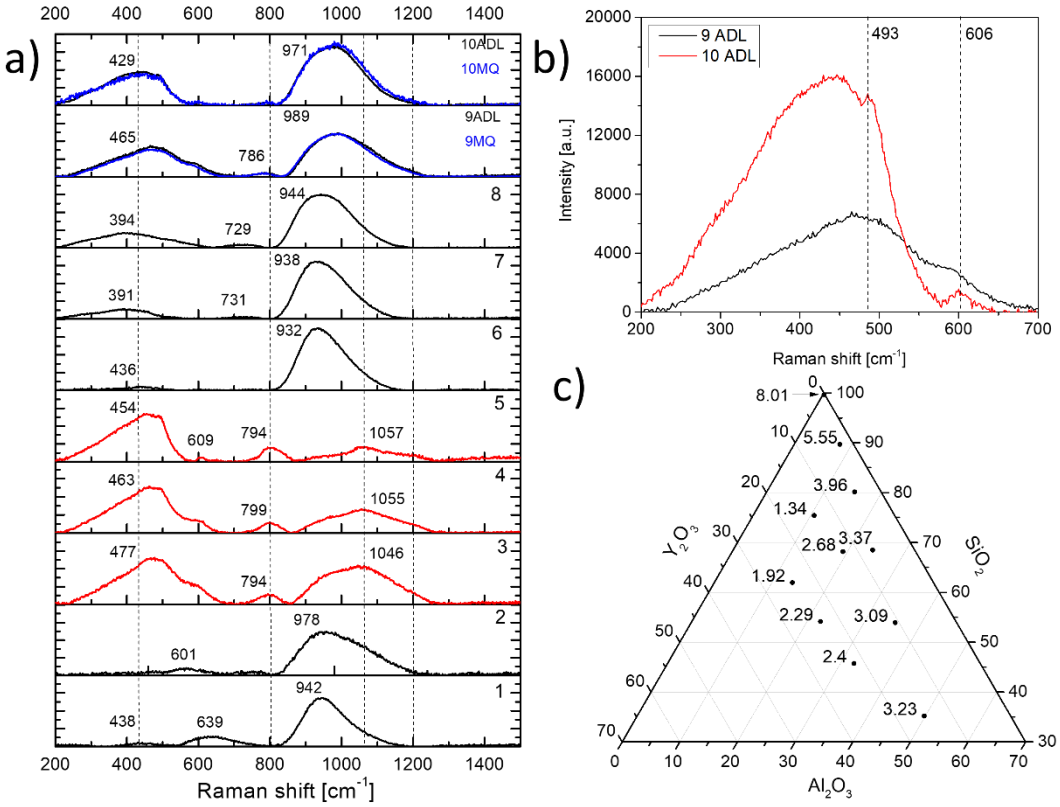

Figure 5 *Raman spectra of the samples prepared by ADL a) spectra comparison – the vertical dashed lines correspond to the 430, 800, 1060 and 1200cm^{-1} bands assigned to the fundamental vibrations of silicate glasses. They are added for better orientation. Small numbers indicate the maxima of the measured bands; b) a detail of the spectra – a comparison of the glass samples* **9** *(Y13-A19-S68) and* ***10*** *(Y14-A11-S75), prepared by ADL; c) the degree of glass polymerisation on a part of the YAS ternary diagram (mol%).*

They are also indicated in the spectra of the glass with the compositions **4** (*Y05-A15-S80*) and **5** (*Y02-A08-S90*) with a very high SiO_2 content. These bands are located at 493 and 606 cm^{-1}; they are typical of the spectrum of pure SiO_2 and have been assigned to defects in the glass structure, associated with the breathing vibrations of oxygen atoms in four- and three-membered tetrahedral rings [55,56].

The degree of glass polymerisation can be qualitatively evaluated as the intensity ratio of the regions associated with the Si–BO bending vibrations (A_{500}) and to the Si-O-Si stretching (A_{1000}) bands [57]. The average value of A_{500}/A_{1000} has been calculated from the five spectra recorded at the same spot of each glass sample. The average values of the degree of polymerisation (A_{500}/A_{1000}) of the glass used have been calculated using a standard process (see e.g. [18]). **Figure 5c** shows the change in the degree of polymerisation calculated for each glass in the ternary diagram. It is evident from this figure that the degree of network polymerisation increases with the addition of SiO_2, as expected, but simultaneously also with the addition of Al_2O_3, which is an intermediary oxide and may act as both a network former

and a network modifier. An increase of Al_2O_3 content thus leads to the incorporation of Al^{3+} in network-forming four-fold coordination. The content of Y_2O_3 as a modifier seems to reduce the degree of glass-network polymerisation.

3.3. The investigation of phase separation in the glass prepared

Since there were no clear differences between XRD and Raman analyses when comparing the samples **9** (*Y13-A19-S68*) (transparent) and **10** (*Y14-A11-S75*) (white opaque), the samples with these compositions as well as samples containing more than 65 mol% of SiO_2 were characterised using electron microscopy. SEM images were collected using backscattered electrons, so that areas containing a higher concentration of heavy elements (such as Y^{3+}) appeared brighter. On the contrary, TEM images were acquired in the bright-field mode: due to the fully amorphous state of the samples, the contrast arose from density fluctuations, with denser phases appearing darker.

The sample **9** (*Y13-A19-S68*) appeared fully homogeneous down to the nanoscale level according to TEM examination (**Figure 6**), after both ADL and conventional melt-quenching synthesis. On the contrary, the sample **10** (*Y14-A11-S75*) exhibited an amorphous phase separation during SEM inspection, with darker nanoparticles (SiO_2-enriched according to EDS analyses) in a brighter matrix. The nanoparticles appeared bigger in the melt-quenched sample, reaching the maximum diameter of approximately 200 nm, while they reached ca 50 nm in the ADL sample. This size difference is likely to arise from the different melting temperature and quenching rate of the materials during the synthesis [58].

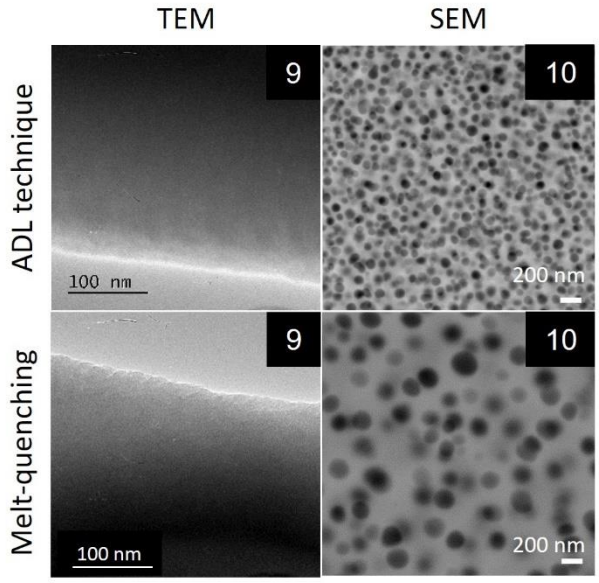

Figure 6 *Electron microscopy images (SEM and TEM) – a comparison of the microstructure of the samples prepared by melt-quenching and ADL.*

Subsequently, the samples prepared by ADL within the liquid–liquid immiscibility field [29,33] were characterised by SEM to gain more insight into the morphology of their amorphous phase separation. The samples **11** (*Y08-A12-S80*), **12** (*Y06-A09-S85*), **13** (*Y04-A06-S90*) and **14** (*Y02-A03-S95*) demonstrate that an increasing content of SiO_2 leads to a decrease of the nanoparticle size (**Figure 7a**). In the glass **11** (*Y08-A12-S80*), most of the particles have the size of 50–60 nm, whereas in the glass **14** (*Y02-A03-S95*), the nanoparticles exhibit the size of 30–40 nm. The decreasing imaging contrast between the particles and the matrix may also indicate a decreasing difference in their chemical composition.

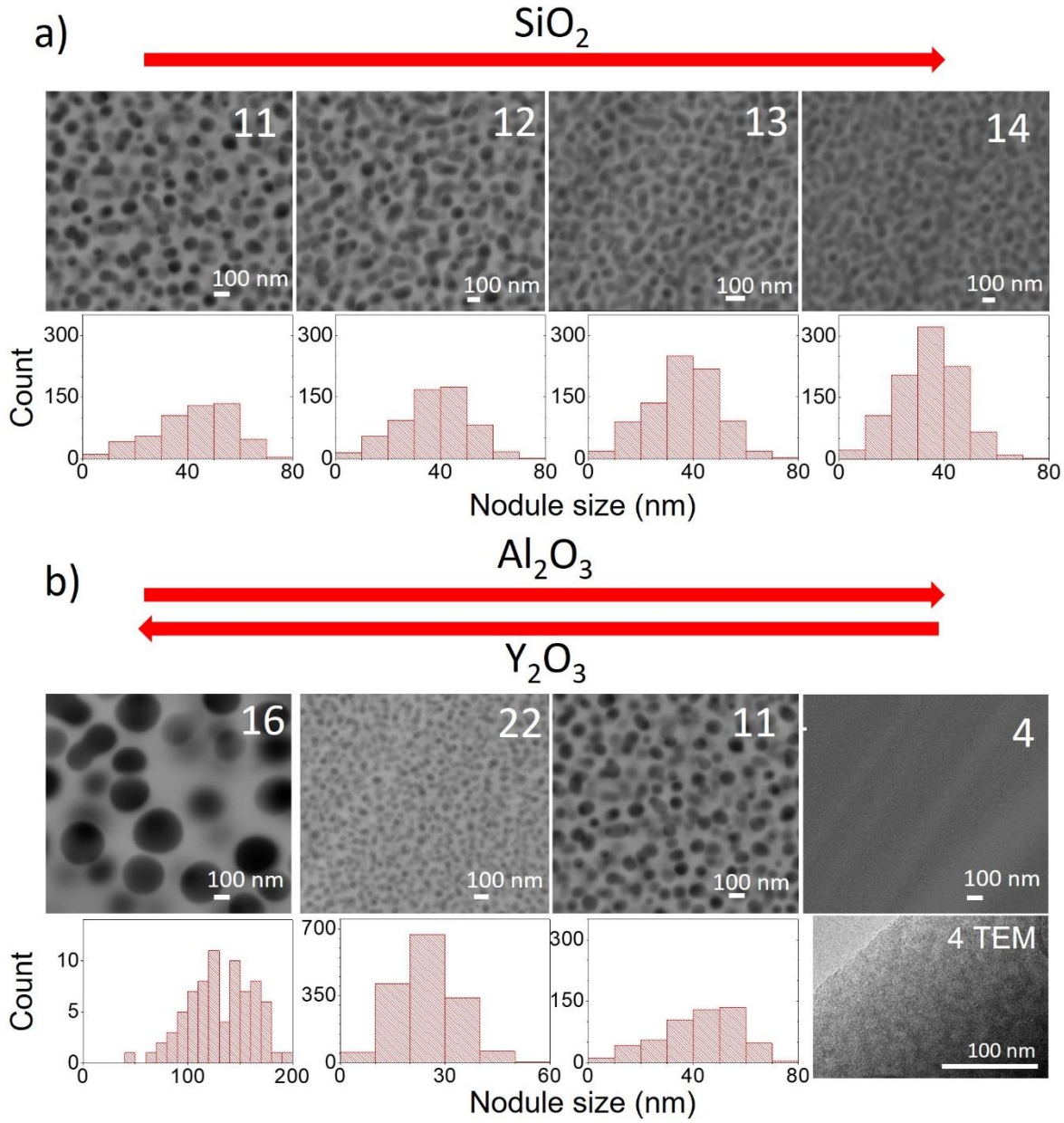

Figure 7 *The influence of chemical composition on the microstructure of phase-separated glass –SEM images: a) increasing SiO_2, b) increasing Al_2O_3 and decreasing Y_2O_3. Since the SEM image of the sample 4 does not show any* ***nanoparticles****, a TEM image of this sample is presented instead of the*

histogram, showing signs of spinodal decomposition. All bins in the histograms represent a particle-diameter difference of 10 nm.

Consequently, the effect of Al_2O_3 addition and the simultaneous reduction of Y_2O_3 content has also been investigated (from left to right in the phase diagram). The glass samples marked as **16** (*Y15-A05-S80*), **22** (*Y10-A10-S80*), **11** (*Y08-A12-S80*) and **4** (*Y05-A15-S80*) have been prepared. SEM images are shown in **Figure 7b**. The growth or reduction of glass phase nanoparticles is not as systematic as before. Large nanoparticles (some with a diameter of up to 180 nm) become small (30–50 nm) with the addition of Al_2O_3. Good contrast is still evident and the prepared glass exhibits opalescence. With the addition of a higher amount of Al_2O_3, the size increases again to an average of 40–60 nm simultaneously with a decrease in contrast. After another addition of Al_2O_3, the observed glass-phase separation disappears completely (sample **4**). Under TEM, signs of spinodal decomposition can be observed in this sample.
In order to study the interesting changes in the microstructure caused by Al_2O_3 addition as well as to determine the chemical composition of the nanoparticles, selected samples were additionally inspected by high-resolution TEM. Compared to the SEM analysis (**Figure 7**), the nanoparticles are depicted in reverse contrast and are lighter than the matrix. The sample **22** (*Y10-A10-S80*) was prepared as a thin lamella, whereas the samples **16** (*Y15-A05-S80*) and **12** (*Y06-A09-S85*) were analysed as powder. **Figure 8** shows the images obtained. The first row shows only the images of the glass **22** (*Y10-A10-S80*) (opalescent sample). The glass presents a phase separation with small (with the average diameter being around 66 nm) brighter nanoparticles in a dark matrix. When examined in detail, local interconnection between several nanoparticles is sometimes evident. The electron-diffraction pattern does not show defined spots, indicating an amorphous state. Consequently, the compositions of both the nanoparticles and the matrix were determined by EDS analyses (see **Table 3**). The absolute measurement error is less than ±1%. The error might be largely caused by the superposition of the nanoparticles analysed and the matrix.

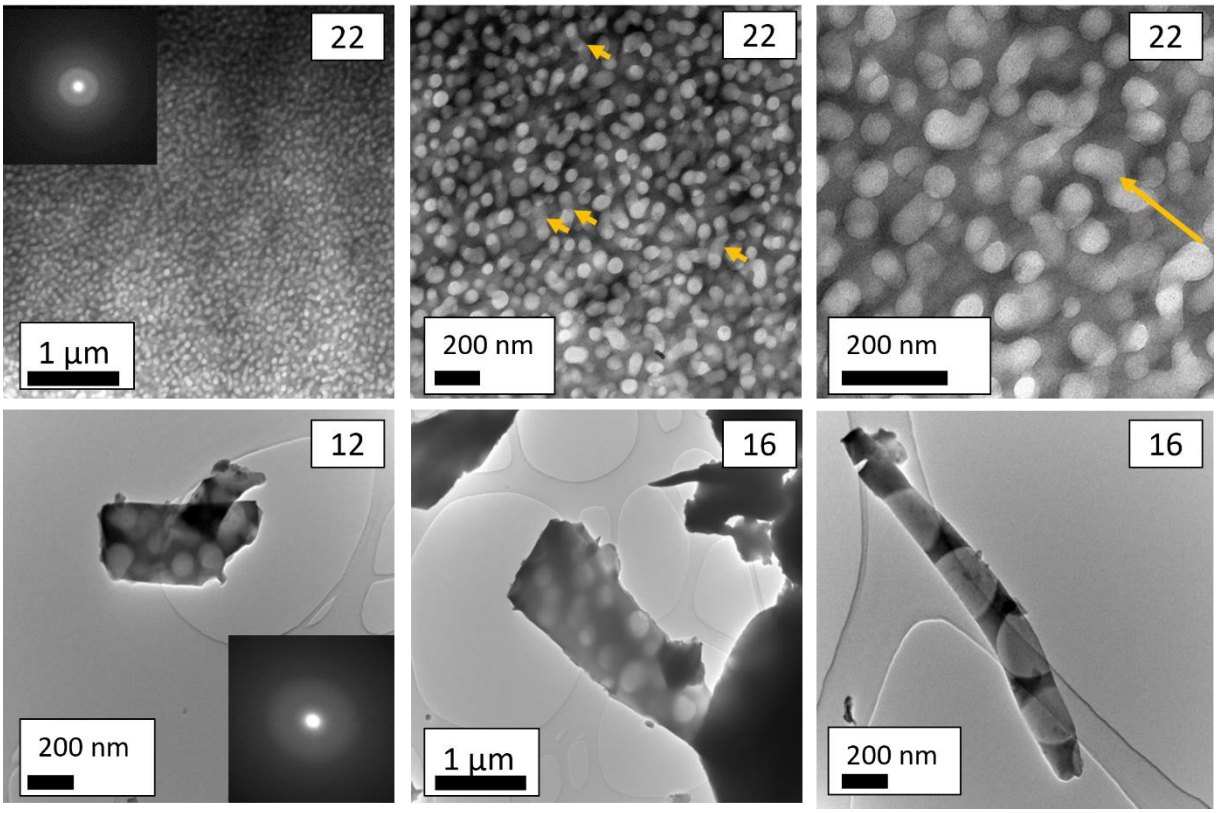

Figure 8 *TEM images of the samples 22, 12 and 16. The orange arrows point at the 'channels' between the white nanoparticles in the opalescent sample 22. The electron diffraction patterns indicate an amorphous state.*

The second row in **Figure 8** shows images of the samples **12** (*Y06-A09-S85*) and **16** (*Y15-A05-S80*), with the same kind of phase separation with white nanoparticles in a darker matrix. The spherical nanoparticles seem to be well separated. The average diameter is 105 nm for the sample **12** (*Y06-A09-S85*) and 327 nm for the sample **16** (*Y15-A05-S80*). These diameters are in good agreement with the spherical nanoparticles distribution investigated by SEM. Again, electron diffraction patterns have confirmed the amorphous state of the material, with the absence of any bright spots or reflections. It is clear from the results of the EDS analysis (see **Table 3**) that the nanoparticles in all samples have the same composition, close to pure SiO_2, whereas the glass matrix reflects very well the trend and ratios of the oxides from the nominal bulk composition.

Table 3 *The chemical composition of the samples 12, 16 and 22 in mol%. The absolute measurement error is less than ±1%.*

Sample	***Matrix***			***Nodules***		
	Y_2O_3	Al_2O_3	SiO_2	Y_2O_3	Al_2O_3	SiO_2
12	21.0	13.5	65.5	1.0	1.5	97.5
16	28.5	7.5	64.0	1.0	1.0	98.0
22	15.5	14.0	70.5	1.0	1.5	97.5

4. Discussion

Most of the existing publications on nanostructured materials in the YAS system have mainly focused on the formation of crystalline nanoparticles, which are formed by the subsequent annealing of the glass of a given composition [53–55]. In the glass-forming region of the phase diagram, there are commonly crystalline SiO_2, $Y_2Si_2O_7$, $3Al_2O_3{\cdot}2SiO_2$ (mullite) and Al_2O_3 [38,39]. These phases are mostly irregular in shape due to crystallisation and their low symmetry. Crystalline phases rarely have a spherical shape. On the contrary, our work demonstrates the potential (and limitations) of exploiting liquid–liquid phase separation for the preparation of nanostructured materials containing amorphous spherical SiO_2 nanoparticles in the YAS system. Concerning the size, distribution and chemical composition of the nanoparticles formed, the following facts are evident from the above-mentioned results:

i) Only amorphous nanoparticles with a composition very close to pure SiO_2 can be formed in the investigated region of the YAS system.

ii) Nanoparticles are formed if the melt contains 75 or more mol% of SiO_2 and simultaneously around 20 or less mol% of Y_2O_3.

iii) Changes in the Y/Al ratio of the samples significantly affect the size of SiO_2-enriched nanoparticles, but the change is not directly proportional to the composition.

iv) Changes in the SiO_2 content seem to have a less significant effect on the size and composition of the nanoparticles. An increase in the overall SiO_2 content of the melt has probably led to a SiO_2 enrichment of the matrix, which has approached the composition of the nanoparticles (as can be inferred from the lower contrast in **Figure 7**).

v) With the identical content of both Y_2O_3 and Al_2O_3, opalescent glass has been formed in the region above 65 mol% of SiO_2, which is characterised by a very small size of SiO_2 nanoparticles and also some interconnection between the nanoparticles.

If we compare the two chosen technologies, the influence of the synthesis used (ADL or conventional melt quenching) is obvious. The two methods differ mainly in the maximum achievable melting temperature and the cooling rate. It is a well-known fact that a higher cooling rate leads to the formation of a larger number of small nanoparticles and vice versa [58]. This fact has been confirmed and is evident in the comparison of the preparation of the glass **10** (Y14-A11-S75) (see **Figure 6**), where the SiO_2 nanoparticles formed using the ADL technology are smaller than in the case of the MQ technology.

As far as the description of the YAS phase system is concerned, the experimental data on it are sparse and contradictory; for example, the phase diagrams of this system calculated by Groebner [40] are inconsistent with more recent data [32] on subsolidus phase relations. New calorimetric measurements and calculations especially in the near-eutectic region have been reported in [39]. The region of the phase diagram with SiO_2 content above 70 mol% is practically unexplored – most authors report the formation of crystalline SiO_2 (tridymite). Theoretical models are given by Pan et al. [29], mentioned above, and Mao et al. [33], who define the phase separation region above 70 mol% of SiO_2; these are in

reasonably good agreement with our experimental results. The region defined by Mao et al. [33] corresponds to the region where spherical SiO_2-enriched nanoparticles are formed as a result of phase separation, according to our observations. The region defined by Mao is also characterised by obvious phase separation, which may not manifest itself as spherical SiO_2 formations but as spinodal decomposition.

Regarding the shape and composition of the resulting nanoparticles, similar amorphous and spherical nanoparticles have been observed in the YAS system mainly during the drawing of optical fibres. In fact, the method of drawing optical fibres is a similar technology to ADL, because the glass is cooled very rapidly from the high melting temperature, which allows the formation of amorphous nanoparticles. Indeed, nanostructured optical fibres have previously been described in the YAS system especially by Paul et al., while nanoparticles with the size of 5–10 nm have been reported in YAS preforms and fibres, with a high content of SiO_2 (>90 mol%) [59,62–66], where their size as well as distribution were controlled by the presence of phosphorus or fluorine. Paul et al. first crystallised YAG nanocrystals in the preform, which were then amorphised by drawing. The amorphous nanoparticles or parts with spinodal decomposition were significantly enriched by Y_2O_3 and Al_2O_3 or another dopant used, whereas the surrounding matrix was enriched by silica [67,68]. In our work, on the other hand, the nanoparticles have been formed by phase separation: their spherical shape is in agreement with previous results, but the nanoparticles prepared in our experiments contain practically pure SiO_2, while other oxides such as Y_2O_3 and Al_2O_3 have enriched the space between the nanoparticles. Our results are rather in agreement with the description of the La_2O_3-Al_2O_3-SiO_2 (LAS) system, where the authors consistently found phase separation for low values of Al/Si atomic ratio and confirmed silicate as well as depolymerised lanthanum-silicate regions weakly substituted by aluminium, in addition to spherical nanoparticles with a high SiO_2 content [69,70].

5. Conclusion

Our results shed new light on liquid–liquid phase separation in the YAS system, specifically in the region with 65 or more mol% of SiO_2 and simultaneously with the maximum of 17.5 mol% of Y_2O_3. In this region, SiO_2 nano-sized amorphous nanoparticles are formed. As expected, the size and distribution of these nanoparticles can be controlled by the synthesis technology used, i.e. by the cooling rate. Slow cooling (melt-quenching) produces bigger nanoparticles than very fast cooling (ADL). In addition, the formation and size of the nanoparticles can also be fundamentally influenced by the composition. An increase in SiO_2 reduces the compositional contrast between the nanoparticles and the matrix, probably because of a lower driving force towards phase separation. Conversely, an increase in the glass modifier Y_2O_3 results in the formation of SiO_2 nanoparticles of different sizes, which can vary from tens to hundreds of nanometres depending on its content. With the equal content of Y_2O_3 and Al_2O_3, it is possible to prepare an opalescent sample with very small, interconnected nanoparticles. In conclusion,

this work could be used as a guide for the tuneable creation of SiO_2 spherical nanoparticles in YAS glass for various potential applications.

CRediT author statement

Jan Baborák: conceptualisation, methodology, investigation, formal analysis, data curation, writing – the original draft, sample preparation; **Petr Vařák**: Raman data evaluation, investigation; **Aurélien Canizares:** Raman data acquisition, consulting, **Miroslav Rada:** melt-quenching expertise and sample preparation; **Cécile Genevois:** TEM data acquisition and evaluation; **Michael J. Pitcher:** conceptualisation, supervision, review; **Emmanuel Véron:** XRD and SEM data acquisition, supervision, review; **Alessio Zandonà:** conceptualisation, writing, editing, literature research, review; **Mathieu Allix:** conceptualisation, methodology, supervision, funding acquisition, writing – review & editing, investigation; **Pavla Nekvindová:** conceptualisation, methodology, supervision, funding acquisition, writing – review & editing, investigation.

Declaration of competing interests

The authors declare that they have no known competing financial interests or personal relationships that could have appeared to influence the work reported in this paper.

Acknowledgements

This project has benefited from the expertise and facilities of the Platform MACLE-CVL, which has been co-funded by the European Union and the Centre-Val de Loire Region (FEDER). This work has been supported by the Czech Science Foundation (GACR), project number GA23-05507S. Jan Baborak wishes to acknowledge the Barrande Fellowship Program coordinated by the French Institute in Prague (IFP) and the Czech Ministry of Education, Youth and Sports (MEYS). The authors thank the ICMN Laboratory (Orléans, France) for TEM access.

References

[1] I. Konidakis, A. Karagiannaki, E. Stratakis, Advanced composite glasses with metallic, perovskite, and two-dimensional nanocrystals for optoelectronic and photonic applications, Nanoscale. 14 (2022) 2966–2989. https://doi.org/10.1039/D1NR07711B.

[2] M.S. Rider, Á. Buendía, D.R. Abujetas, P.A. Huidobro, J.A. Sánchez-Gil, V. Giannini, Advances and Prospects in Topological Nanoparticle Photonics, ACS Photonics. 9 (2022) 1483–1499. https://doi.org/10.1021/acsphotonics.1c01874.

[3] R. Klement, K. Drdlíková, D. Drdlík, K. Maca, Photoluminescence of rare-earth/transition metal-doped transparent/translucent polycrystalline Al_2O_3 ceramics: A review, J. Am. Ceram. Soc. 106 (2023) 172–185. https://doi.org/10.1111/jace.18618.

[4] W. Blanc, Z. Lu, T. Robine, F. Pigeonneau, C. Molardi, D. Tosi, Nanoparticles in optical fiber, issue and opportunity of light scattering [Invited], Opt. Mater. Express. 12 (2022) 2635. https://doi.org/10.1364/OME.462822.

[5] P. Vařák, M. Kamrádek, J. Mrázek, O. Podrazký, J. Aubrecht, P. Peterka, P. Nekvindová, I. Kašík, Luminescence and laser properties of RE-doped silica optical fibers: The role of composition, fabrication processing, and inter-ionic energy transfers, Opt. Mater. X. 15 (2022) 100177. https://doi.org/10.1016/j.omx.2022.100177.

[6] R. Won, Ceramic future, Nat. Photonics. 2 (2008) 216–217. https://doi.org/10.1038/nphoton.2008.46.

[7] X. Ma, X. Li, J. Li, C. Genevois, B. Ma, A. Etienne, C. Wan, E. Véron, Z. Peng, M. Allix, Pressureless glass crystallization of transparent yttrium aluminum garnet-based nanoceramics, Nat. Commun. 9 (2018) 1175. https://doi.org/10.1038/s41467-018-03467-7.

[8] I. Savelii, L. Bigot, B. Capoen, C. Gonnet, C. Chanéac, E. Burova, A. Pastouret, H. El-Hamzaoui, M. Bouazaoui, Benefit of Rare-Earth "Smart Doping" and Material Nanostructuring for the Next Generation of Er-Doped Fibers, Nanoscale Res. Lett. 12 (2017) 206. https://doi.org/10.1186/s11671-017-1947-6.

[9] P. Vařák, J. Mrázek, A.A. Jasim, S. Bysakh, A. Dhar, M. Kamrádek, O. Podrazký, I. Kašík, I. Bartoň, P. Nekvindová, Thermal stability and photoluminescence properties of RE-doped (RE = Ho, Er, Tm) alumina nanoparticles in bulk and fiber-optic silica glass, Opt. Mater. 118 (2021) 111239. https://doi.org/10.1016/j.optmat.2021.111239.

[10] P.H. Reddy, S. Das, D. Dutta, A. Dhar, A.V. Kir'yanov, M. Pal, S.K. Bhadra, M.C. Paul, Luminescent Properties and Optical Amplification of Erbium-Doped Nano-Engineered Scandium-Phospho-Yttria-Alumina-Silica Glass Based Optical Fiber, Phys. Status Solidi A. 215 (2018) 1700615. https://doi.org/10.1002/pssa.201700615.

[11] G. Brasse, C. Restoin, J.-L. Auguste, S. Hautreux, J.-M. Blondy, A. Lecomte, Nanostructured optical fiber by the sol-gel process in the SiO2–ZrO2 system, Appl. Phys. Lett. 91 (2007) 121920. https://doi.org/10.1063/1.2786604.

[12] A. Dhar, I. Kasik, B. Dussardier, O. Podrazky, V. Matejec, Preparation and Properties of Er-Doped ZrO2 Nanocrystalline Phase-Separated Preforms of Optical Fibers by MCVD Process, Int. J. Appl. Ceram. Technol. 9 (2012) 341–348. https://doi.org/10.1111/j.1744-7402.2011.02669.x.

[13] P. Vařák, J. Mrázek, W. Blanc, J. Aubrecht, M. Kamrádek, O. Podrazký, Preparation and properties of Tm-doped SiO_2 -ZrO_2 phase separated optical fibers for use in fiber lasers, Opt. Mater. Express. 10 (2020) 1383. https://doi.org/10.1364/OME.394068.

[14] O. Dymshits, E. Gorokhova, I. Alekseeva, V. Golubkov, M. Shepilov, A. Khubetsov, M. Tsenter, D. Shemchuk, A. Bachina, A. Volokitina, L. Basyrova, M. Baranov, E. Oreschenko, X. Mateos, P. Loiko, A. Zhilin, Transparent materials based on semiconducting ZnO: glass-ceramics and

optical ceramics doped with rare-earth and transition-metal ions, J. Non-Cryst. Solids. 588 (2022) 121625. https://doi.org/10.1016/j.jnoncrysol.2022.121625.

[15] B. Ghaemi, G. Zhao, S. Huang, J. Wang, G. Han, Structural and Luminescence Properties of Er-Doped Zinc-Alumino-Silicate Glass Ceramic, J. Am. Ceram. Soc. 95 (2012) 1911–1914. https://doi.org/10.1111/j.1551-2916.2012.05200.x.

[16] G. Granger, C. Restoin, P. Roy, R. Jamier, S. Rougier, A. Lecomte, J.-M. Blondy, Nanostructured optical fibers in the SiO2/SnO2 system by the sol-gel method, Mater. Lett. 120 (2014) 292–294. https://doi.org/10.1016/j.matlet.2014.01.104.

[17] S. Chenu, emmanuel veron, C. Genevois, alain garcia, guy matzen, M. Allix, Long-lasting luminescent ZnGa2O4:Cr3+ transparent glass-ceramics, J. Mater. Chem. C. 2 (2014). https://doi.org/10.1039/C4TC02081B.

[18] M.-I. Chen, A. Singh, J.-L. Chiang, R.-H. Horng, D.-S. Wuu, Zinc Gallium Oxide—A Review from Synthesis to Applications, Nanomaterials. 10 (2020) 2208. https://doi.org/10.3390/nano10112208.

[19] S. G., D. Hebbar N., S.G. Menon, P.M. Lewis, K.S. Choudhari, R.E. Kroon, H.C. Swart, S.D. Kulkarni, Cr-doped ZnGa2O4: Simple synthesis of intense red-NIR emitting nanoparticles with enhanced quantum efficiency, Opt. Mater. 123 (2022) 111919. https://doi.org/10.1016/j.optmat.2021.111919.

[20] D. Nathiya, N.M.I. Alhaji, A.R. Mohamed Jahangir, M. Ismail Fathima, M.K. Gatasheh, A.A. Hatamleh, S. Zehra, A. Ayeshamariam, Synthesis and characterization of ZnGa2O4 composites and its photocatalytic properties for energy applications, Environ. Res. 204 (2022) 112073. https://doi.org/10.1016/j.envres.2021.112073.

[21] C. Mével, J. Carreaud, G. Delaizir, J.-R. Duclère, F. Brisset, J. Bourret, P. Carles, C. Genevois, M. Allix, S. Chenu, First ZnGa2O4 transparent ceramics, J. Eur. Ceram. Soc. 41 (2021) 4934–4941. https://doi.org/10.1016/j.jeurceramsoc.2021.03.038.

[22] M. Wang, Q. Zheng, A. Chen, Y. Li, X. Zhang, D. Zhang, S. Jin, D. Xiong, W. Deng, Crystallization, thermal expansion and hardness of Y2O3–Al2O3–SiO2 glasses, Ceram. Int. 47 (2021) 25059–25066. https://doi.org/10.1016/j.ceramint.2021.05.236.

[23] M.J. Hyatt, D.E. Day, Glass Properties in the Yttria-Alumina-Silica System, J. Am. Ceram. Soc. 70 (1987) C-283-C–287. https://doi.org/10.1111/j.1151-2916.1987.tb04901.x.

[24] A. Prnová, A. Domanická, R. Klement, J. Kraxner, M. Polovka, M. Pentrák, D. Galusek, P. Šimurka, J. Kozánková, Er- and Nd-doped yttrium aluminosilicate glasses: Preparation and characterization, Opt. Mater. 33 (2011) 1872–1878. https://doi.org/10.1016/j.optmat.2011.03.008.

[25] Y. Zhang, J. Qiu, Yttrium aluminosilicate (YAS) fiber with heavily doped of Nd for single frequency laser, in: 2018 Asia Commun. Photonics Conf. ACP, 2018: pp. 1–2. https://doi.org/10.1109/ACP.2018.8595750.

[26] Y. Zhang, G. Qian, X. Xiao, X. Tian, X. Ding, Z. Ma, L. Yang, H. Guo, S. Xu, Z. Yang, J. Qiu, The preparation of Yttrium Aluminosilicate (YAS) Glass Fiber with heavy doping of Tm3+ from Polycrystalline YAG ceramics, J. Am. Ceram. Soc. 101 (2018) 4627–4633. https://doi.org/10.1111/jace.15722.

[27] R. Harrysson, P. Vomacka, Glass formation in the system Y2O3 Al2O3 SiO2 under conditions of laser melting, J. Eur. Ceram. Soc. 14 (1994) 377–381. https://doi.org/10.1016/0955-2219(94)90075-2.

[28] S. Ahmad, T. Ludwig, M. Herrmann, M.M. Mahmoud, W. Lippmann, H.J. Seifert, Phase evaluation during high temperature long heat treatments in the Y2O3–Al2O3–SiO2 system, J. Eur. Ceram. Soc. 34 (2014) 3835–3840. https://doi.org/10.1016/j.jeurceramsoc.2014.05.025.

[29] Z. Pan, O. Fabrichnaya, H. Seifert, R. Neher, K. Brandt, M. Herrmann, Thermodynamic evaluation of the Si-C-Al-Y-O system for LPS-SiC application, J. Phase Equilibria Diffus. 31 (2010). https://doi.org/10.1007/s11669-010-9695-7.

[30] N.A. Toropov, I.A. Bondar', F.Ya. Galadhov, Kh.S. Nikogosyan, N.V. Vinogradova, Phase equilibria in the yttrium oxide-alumina system, Bull. Acad. Sci. USSR Div. Chem. Sci. 13 (1964) 1076–1081. https://doi.org/10.1007/BF00863104.

[31] Y. Zhang, A. Navrotsky, Thermochemistry of Glasses in the Y2O3-Al2O3-SiO2 System, J. Am. Ceram. Soc. 86 (2003) 1727–1732. https://doi.org/10.1111/j.1151-2916.2003.tb03547.x.

[32] U. Kolitsch, H.J. Seifert, T. Ludwig, F. Aldinger, Phase equilibria and crystal chemistry in the Y2O3–Al2O3–SiO2 system, J. Mater. Res. 14 (1999) 447–455. https://doi.org/10.1557/JMR.1999.0064.

[33] H. Mao, M. Selleby, O. Fabrichnaya, Thermodynamic reassessment of the Y 2O3–Al2O3–SiO2 system and its subsystems, Calphad. 32 (2008) 399–412. https://doi.org/10.1016/j.calphad.2008.03.003.

[34] S.H. Risbud, J.A. Pask, Mullite Crystallization from SiO2-Al2O3 Melts, J. Am. Ceram. Soc. 61 (1978) 63–67. https://doi.org/10.1111/j.1151-2916.1978.tb09232.x.

[35] T. Takei, I. Kameshima, A. Yasumori, K. Okada, Crystallization kinetics of mullite in alumina–silica glass fibers, J. Am. Ceram. Soc. 21 (2004) 2487–2493.

[36] M. Hnatko, P. Šajgalík, Z. Lenčéš, D. Salamon, F. Monteverde, Carbon reduction reaction in the Y2O3–SiO2 glass system at high temperature, J. Eur. Ceram. Soc. 21 (2001) 2797–2801. https://doi.org/10.1016/S0955-2219(01)00231-X.

[37] Z. Sun, M. Li, Y. Zhou, ChemInform Abstract: Recent Progress on Synthesis, Multi-Scale Structure, and Properties of Y—Si—O Oxides, ChemInform. 46 (2015). https://doi.org/10.1002/chin.201513295.

[38] N. Sadiki, J.P. Coutures, C. Fillet, J.L. Dussossoy, Crystallization of lanthanum and yttrium aluminosilicate glasses, J. Nucl. Mater. 348 (2006) 70–78. https://doi.org/10.1016/j.jnucmat.2005.09.003.

[39] O. Fabrichnaya, H.J. Seifert, R. Weiland, T. Ludwig, F. Aldinger, A. Navrotsky, Phase Equilibria and Thermodynamics in the Y2O3–Al2O3–SiO2 System, Int. J. Mater. Res. 92 (2001) 1083–1097. https://doi.org/10.3139/ijmr-2001-0197.

[40] J. Groebner, Constitution Calculations in the System Y–Al–Si–C–O, University of Stuttgart, 1994.

[41] L.B. Skinner, A.C. Barnes, W. Crichton, Novel behaviour and structure of new glasses of the type Ba–Al–O and Ba–Al–Ti–O produced by aerodynamic levitation and laser heating, J. Phys. Condens. Matter. 18 (2006) L407–L414. https://doi.org/10.1088/0953-8984/18/32/L01.

[42] A. Zandonà, M. Moustrous, C. Genevois, E. Véron, A. Canizarès, M. Allix, Glass-forming ability and ZrO2 saturation limits in the magnesium aluminosilicate system, Ceram. Int. 48 (2022) 8433–8439. https://doi.org/10.1016/j.ceramint.2021.12.051.

[43] J. Baborák, M. Yembele, P. Vařák, S. Ory, E. Véron, M.J. Pitcher, M. Allix, P. Nekvindová, A. Zandonà, Key melt properties for controlled synthesis of glass beads by aerodynamic levitation coupled to laser heating, Int. J. Appl. Glass Sci. 14 (2023) 455–467. https://doi.org/10.1111/ijag.16627.

[44] U.C. Paek, C.R. Kurkjian, Calculation of Cooling Rate and Induced Stresses in Drawing of Optical Fibers, J. Am. Ceram. Soc. 58 (1975) 330–335. https://doi.org/10.1111/j.1151-2916.1975.tb11490.x.

[45] B. Svecova, J. Spirkova, P. Nekvindova, M. Mika, L. Svecova, Ion exchange as a new tool to evaluate and quantify glass homogeneity, J. Non-Cryst. Solids. 356 (2010) 1509–1513. https://doi.org/10.1016/j.jnoncrysol.2010.03.014.

[46] J.K. Christie, A. Tilocca, Aluminosilicate Glasses As Yttrium Vectors for in situ Radiotherapy: Understanding Composition-Durability Effects through Molecular Dynamics Simulations, Chem. Mater. 22 (2010) 3725–3734. https://doi.org/10.1021/cm100847p.

[47] T. Schaller, J.F. Stebbins, The Structural Role of Lanthanum and Yttrium in Aluminosilicate Glasses: A ^{27} Al and ^{17} O MAS NMR Study, J. Phys. Chem. B. 102 (1998) 10690–10697. https://doi.org/10.1021/jp982387m.

[48] E.M. Erbe, D.E. Day, Chemical durability of Y2O3-Al2O3-SiO2 glasses for thein vivo delivery of beta radiation, J. Biomed. Mater. Res. 27 (1993) 1301–1308. https://doi.org/10.1002/jbm.820271010.

[49] P. McMillan, A Raman spectroscopic study of glasses in the system CaO–MgO–SiO2, Am. Mineral. 69 (1984) 645–659.

[50] D.W. Matson, S.K. Sharma, J.A. Philpotts, The structure of high-silica alkali-silicate glasses. A Raman spectroscopic investigation, J. Non-Cryst. Solids. 58 (1983) 323–352. https://doi.org/10.1016/0022-3093(83)90032-7.

[51] C. O'Shaughnessy, G.S. Henderson, H.W. Nesbitt, G.M. Bancroft, D.R. Neuville, The influence of modifier cations on the Raman stretching modes of Qn species in alkali silicate glasses, J. Am. Ceram. Soc. 103 (2020) 3991–4001. https://doi.org/10.1111/jace.17081.

[52] C. Huang, E.C. Behrman, Structure and properties of calcium aluminosilicate glasses, J. Non-Cryst. Solids. 128 (1991) 310–321. https://doi.org/10.1016/0022-3093(91)90468-L.

[53] S. Petrescu, M. Constantinescu, E.M. Anghel, I. Atkinson, M. Olteanu, M. Zaharescu, Structural and physico-chemical characterization of some soda lime zinc alumino-silicate glasses, J. Non-Cryst. Solids. 358 (2012) 3280–3288. https://doi.org/10.1016/j.jnoncrysol.2012.09.001.

[54] D.R. Neuville, L. Cormier, V. Montouillout, P. Florian, F. Millot, J.-C. Rifflet, D. Massiot, Amorphous materials: Properties, structure, and durability: Structure of Mg- and Mg/Ca aluminosilicate glasses: 27Al NMR and Raman spectroscopy investigations, Am. Mineral. 93 (2008) 1721–1731. https://doi.org/10.2138/am.2008.2867.

[55] R.A. Barrio, F.L. Galeener, E. Martínez, R.J. Elliott, Regular ring dynamics in AX 2 tetrahedral glasses, Phys. Rev. B. 48 (1993) 15672–15689. https://doi.org/10.1103/PhysRevB.48.15672.

[56] A.G. KALAMPOUNIAS, IR and Raman spectroscopic studies of sol–gel derived alkaline-earth silicate glasses, Bull. Mater. Sci. 34 (2011) 299–303. https://doi.org/10.1007/s12034-011-0064-x.

[57] P. Colomban, A. Tournie, L. Bellot-Gurlet, Raman identification of glassy silicates used in ceramics, glass and jewellery: a tentative differentiation guide, J. Raman Spectrosc. 37 (2006) 841–852. https://doi.org/10.1002/jrs.1515.

[58] S. Chenu, E. Véron, C. Genevois, G. Matzen, T. Cardinal, A. Etienne, D. Massiot, M. Allix, Tuneable Nanostructuring of Highly Transparent Zinc Gallogermanate Glasses and Glass-Ceramics, Adv. Opt. Mater. 2 (2014) 364–372. https://doi.org/10.1002/adom.201400007.

[59] E. Paul, Intrinsic Point Defects in Zinc Oxide: Modeling of Structural, Electronic, Thermodynamic and Kinetic Properties, Ph.D. Thesis, Technischen Universität Darmstadt, 2006.

[60] S. Fujita, S. Tanabe, Fabrication, microstructure and optical properties of Er3+:YAG glass–ceramics, Opt. Mater. 32 (2010) 886–890. https://doi.org/10.1016/j.optmat.2010.01.014.

[61] H. Dong, Y. Chen, Y. Jiao, Q. Zhou, Y. Cheng, H. Zhang, Y. Lu, S. Wang, C. Yu, L. Hu, Nanocrystalline Yb:YAG-Doped Silica Glass with Good Transmittance and Significant Spectral Performance Enhancements, Nanomaterials. 12 (2022) 1263. https://doi.org/10.3390/nano12081263.

[62] M.C. Paul, S. Bysakh, S. Das, S.K. Bhadra, M. Pal, S. Yoo, M.P. Kalita, A.J. Boyland, J.K. Sahu, Yb2O3-doped YAG nano-crystallites in silica-based core glass matrix of optical fiber preform, Mater. Sci. Eng. B. 175 (2010) 108–119. https://doi.org/10.1016/j.mseb.2010.07.013.

[63] F. d'Acapito, W. Blanc, B. Dussardier, Different Er3+ environments in Mg-based nanoparticle-doped optical fibre preforms, J. Non-Cryst. Solids. 401 (2014) 50–53. https://doi.org/10.1016/j.jnoncrysol.2013.12.040.

[64] M. Cabié, T. Neisius, W. Blanc, Combined FIB/SEM tomography and TEM analysis to characterize high aspect ratio Mg-silicate particles inside silica-based optical fibres, Mater. Charact. 178 (2021) 111261. https://doi.org/10.1016/j.matchar.2021.111261.

[65] M. Vermillac, J.-F. Lupi, F. Peters, M. Cabié, P. Vennéguès, C. Kucera, T. Neisius, J. Ballato, W. Blanc, Fiber-draw-induced elongation and break-up of particles inside the core of a silica-based optical fiber, J. Am. Ceram. Soc. 100 (2017) 1814–1819.

[66] M.C. Paul, S. Bysakh, S. Das, A. Dhar, M. Pal, S.K. Bhadra, J.K. Sahu, A.V. Kir'yanov, F. d'Acapito, Recent Developments in Rare-Earths Doped Nano-Engineered Glass Based Optical Fibers for High Power Fiber Lasers, Trans. INDIAN Ceram. Soc. 75 (2016) 195–208. https://doi.org/10.1080/0371750X.2016.1251852.

[67] V. Fuertes, N. Grégoire, P. Labranche, S. Gagnon, R. Wang, Y. Ledemi, S. LaRochelle, Y. Messaddeq, Engineering nanoparticle features to tune Rayleigh scattering in nanoparticles-doped optical fibers, Sci. Rep. 11 (2021) 9116. https://doi.org/10.1038/s41598-021-88572-2.

[68] T. Cheng, M. Liao, X. Xue, J. Li, W. Gao, X. Li, D. Chen, S. Zheng, Y. Pan, T. Suzuki, Y. Ohishi, A silica optical fiber doped with yttrium aluminosilicate nanoparticles for supercontinuum generation, Opt. Mater. 53 (2016) 39–43. https://doi.org/10.1016/j.optmat.2016.01.018.

[69] S. Iftekhar, J. Grins, M. Edén, Composition–property relationships of the La2O3–Al2O3–SiO2 glass system, J. Non-Cryst. Solids. 356 (2010) 1043–1048. https://doi.org/10.1016/j.jnoncrysol.2010.01.017.

[70] B. Diallo, M. Allix, E. Véron, V. Sarou-Kanian, I. Bardez-Giboire, V. Montouillout, N. Pellerin, Deconvolution method of 29Si MAS NMR spectra applied to homogeneous and phase separated lanthanum aluminosilicate glasses, J. Non-Cryst. Solids. 503–504 (2019) 352–365. https://doi.org/10.1016/j.jnoncrysol.2018.10.026.